Electrooptics of mm-scale polar domains in the ferroelectric nematic phase

Nerea Sebastián, Richard J Mandle, Andrej Petelin, Alexey Eremin & Alenka Mertelj

View supplementary material

Published online: 27 Jul 2021.

Submit your article to this journal

Article views: 2602

View related articles

View Crossmark data

Citing articles: 24 View citing articles

Taylor & Francis
Taylor & Francis Group

∂ OPEN ACCESS ⓡ Check for updates

Electrooptics of mm-scale polar domains in the ferroelectric nematic phase

Nerea Sebastián [ID][a], Richard J Mandle [ID][b], Andrej Petelin[a,c], Alexey Eremin [ID][d] and Alenka Mertelj [ID][a]

aDepartment of Complex Matter, Jožef Stefan Institute, Ljubljana, Slovenia; bSchool of Physics and Astronomy, University of Leeds, Leeds, UK; cFaculty of Mathematics and Physics, University of Ljubljana, Ljubljana, Slovenia; dDepartment of Nonlinear Phenomena, Institute for Physics, Otto Von Guericke University Magdeburg Universitätsplatz 2, Magdeburg, Germany

ABSTRACT

The recent discovery of the ferroelectric nematic phase has opened the door to experimental investigation of one of the most searched liquid crystal phases in decades, with high expectations for future applications. However, at this moment, there are more questions than answers. In this work, we examine the formation and structure of large polar nematic domains of the ferroelectric nematic material RM734 in planar liquid crystals cells with different aligning agents and specifications. We observe that confining surfaces have a strong influence over the formation of different types of domains, resulting in various twisted structures of the nematic director. For those cells predominantly showing mm-scale domains, we investigate the optical and second harmonic generation switching behaviour under applications of electric fields with a special focus on in-plane fields perpendicular to the confinement media rubbing direction. In order to characterise the underlying structure, the polar optical switching behaviour is reproduced using a simplified model together with Berreman calculations.
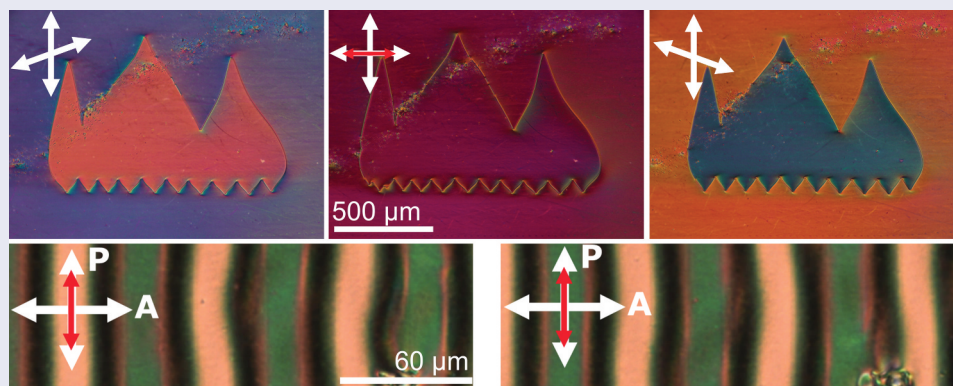
Introduction

A ferroelectric nematic phase is of great fundamental and practical interest. The simplest of the nematic (N) phases, that formed by achiral elongated molecules, does not show any positional order, but on average, molecules orient along the same direction. Such direction, called the director, is represented by a unit vector $\mathbf{n}$, which in the absence of polarity shows head-to-tail symmetry, $\mathbf{n}(\mathbf{r})=-\mathbf{n}(\mathbf{r})$. The possibility of a ferroelectric nematic phase, where the head-to-tail symmetry is broken, was already envisioned by Born [1]. Over the years, it was followed by several theoretical works contemplating the possibility of polar nematic order in discotic liquid crystals (LC) [2,3], or the occurrence of a splayed-polar nematic phase for pear-shaped molecules [4–6].

In the past few years, we have reported a modulated ferroelectric splay nematic phase (N_S), occurring in a material made of slightly wedge-shaped molecules carrying a large dipole moment of ~11.4 D (RM734, see Figure 1) [7–9]. On cooling, RM734 exhibits two distinct nematic phases, separated by a weakly first-order transition [10,11]. In the high temperature N phase, the splay elastic constant rapidly decreases when approaching the $N–N_S$ transition, resulting in a significant pre-transitional behaviour, manifested by strong splay orientational fluctuations. Instability towards splay orientational deformation, arising from the flexoelectric coupling, drives the

a)

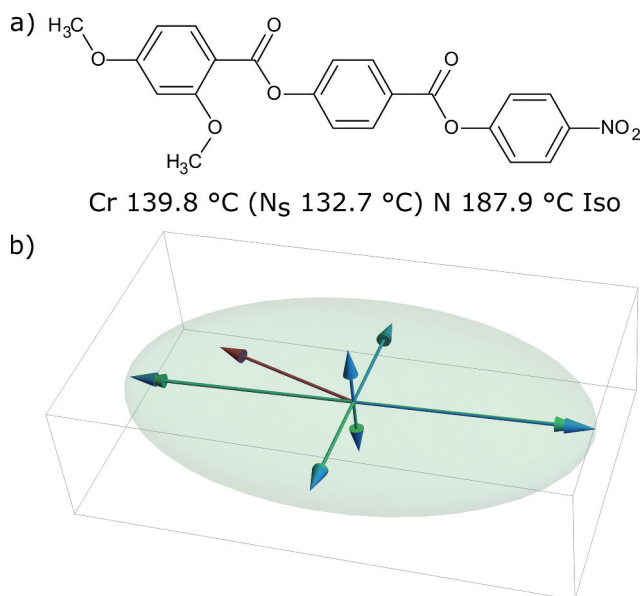Cr 139.8 °C (N$_S$ 132.7 °C) N 187.9 °C Iso

b)

Figure 1. (Colour online) (a) Molecular structure of RM734 and its phase transitions. (b) Representation of dipole moment (red arrow), polarisability tensor at 800 nm (green axis and ellipsoid) and axis of the static polarisability tensor (blue arrows).

transition to a periodically splayed structure. The divergent behaviour of the electric susceptibility shows that it is a paraelectric–ferroelectric phase transition, which, due to the flexoelectric coupling, is accompanied by an orientational ferroelastic transition. The polarity of the splay phase was further proven by second harmonic generation (SHG) imaging, showing that the splay modulation period at the transition is of the order of 5–10 μm. Modulation in the μm range was also reported in a chemically induced N_S phase, in the mixture of two materials which neither of them exhibits the N_S phase: a non-mesogenic bent-core material, which retains some of the features of RM734, and a nematic phase made of molecules analogous in structure to RM734 but with longer terminal chains [12]. Such mixture exhibits the N_S phase at room temperature (8 degrees below the N-N_S transition), for which periodicities ~9 μm have been observed optically. One should note that, particularly in confined geometries and deeper in the N_S, the periodic structure is not the only possibility. Structures can be more complicated and strongly influenced by the boundary conditions, as will be explored in this contribution. Several months later, Chen et al. proposed that the N_S is indeed homogeneous and named it N_F for ferroelectric nematic [13]. They also reported giant spontaneous polarisation of RM734 of P~6 μC/cm^2 measured by means of field-induced current measurements in thin cells [13]. Consistent with the observations for RM734 are those results for the spontaneous polarisation and

SHG in the MP phase initially reported by Nishikawa et al. [14] for a slightly wedge-shaped 1,3-dioxane-based molecule carrying also a large dipole moment (~9.4 D). Very recently Li et al. [15] synthesised a large number of elongated molecules with dipole moments ranging from 4 to 13 D, some exhibiting stable N_F phase (originally named PN for polar Nematic), some metastable N_F and many others no N_F phase at all. Utilising machine-learning analyses they show how molecular parameters such as molecular dipole moment, molecular aspect ratio, molecular length or dipole angle with the molecular axes influence the stabilisation of the polar nematic phase. Interestingly, additionally to a large dipole moment, it appears that a moderate angle (20°) between the molecular axis and the dipole moment is required for the material to exhibit the N_F phase. More recently, R. Saha et al. [16] reported a new highly polar ferroelectric nematic compound for which three distinct ferroelectric phases are reported, which they propose to be N_F, followed by a ferroelectric nematic with short-range hexagonal order (N_{hF}) and lower temperature phase with long-range hexagonal order normal to the director (Col$_{hF}$).

The transition between the N phase and a splayed polar N phase has been extensively described by a Landau-de Gennes type of phenomenological theory [7,8,17], contemplating the flexoelectric coupling between splay deformation and the polar order, similarly to the model for the transition between the nematic and the twist-bend nematic phase of Shamid et al. [18] Very recently, a 2D splay modulation of the director field, together with a 2D modulation of the polar order, has been predicted by Rosseto and Selinger [19]. In their calculations, they show that the 2D structure is in a general energetically more favourable than the 1D modulation, which would only be more favourable in a narrow interval between the uniform nematic and the 2D splay phase. Although this model is good for the description of the phase transition, deeper in the splay phase, the simple description is no longer sufficient, as will be shown below. Because it is not possible to fill the space with uniform splay, a modulated splay structure resembling alternating ferroelectric domains could be a ground state at a given temperature interval. Splay deformation in such a phase would be visible by polarising optical microscopy (POM), if the splay deformation lays in the plane of the layer, a situation, which is typically disfavoured by the homogeneous surface anchoring conditions. The splay deformation would also cause a small optical biaxiality, but because of its smallness compared to birefringence, it would be very difficult to observe it optically. However, the tendency to splay would manifest in the elastic properties, in particular, in the softening of the splay elastic constant,

which is exactly what is observed at the phase transition to the ferroelectric phase [7,8]. The large modulation period observed below the phase transition to the ferroelectric phase, comparable to the standard thicknesses of LC cells (5–20 μm), indicates that the splay deformation is small, and that it is reasonable to anticipate that in a confined system, e.g. such as a typical LC cell, more frustrated structures with similar energies will exist. These structures will be strongly affected by the boundary conditions, and which of these structures will be observed will depend on the history of the sample, e.g. exposure to the external fields, cooling rates, etc.

In this work, we aim to contribute to forming a base of experimental observations for the ferroelectric nematic phase, which will help to further advance in the understanding of this novel nematic phase and to inform the development of theoretical models. Nomenclature of the novel ferroelectric nematic phase (NS, NF, PN, MP) is still controversial and not the subject of this paper. For completeness with our previous contributions on RM734 we will use N_S. We first analyse the formation of different domain structures immediately following the N–N_S phase transition. Furthermore, we examine their electro-optic behaviour under the application of electric fields with special emphasis on in-plane electric fields perpendicularly to **n**, both using POM and SHG imaging (see Methods). We investigate the switching behaviour in the predominant type of domains observed and reproduce it by means of a simplified model and Berreman calculations. The proposed uniform twist structure is finally faced with results from cross-Dynamic Differential Microscopy (c-DDM) [20], which indicate the presence of more complicated underlying twist. This paper is thus organised as follows. Material and results are thoroughly presented in the Results section. Careful examination of them is presented in the Discussion section. Additional material, as the videos corresponding to the results discussed here, is provided in the Supplementary Information (SI).

Methods

Polarising optical microscope

POM experiments were performed in an Optiphot-2 POL Nikon microscope. Images and videos for domain formation and out of plane electric fields were recorded with a Canon EOS100D camera, while experiments in IPS Instec cells were recorded with a CMOS camera (BFLY-U3-23S6C-C). For IPS experiments, the repetition rate of the field profiles was set to 1 Hz and recorded for 400 frames at 15.9 fps. From the video,

the response corresponding to a single cycle was then reconstructed. The sample was held in a heating stage (Instec HCS412W) together with a temperature controller (mK2000, Instec).

Second harmonic generation imaging

SHG imaging was performed using a TCS SP8 Confocal Laser Scanning Microscope (Leica) equipped with a tuneable IR laser and a polarising wheel. Experiments were performed in transmission with the laser excitation with 880 nm. The incoming beam was stopped by a 400/20 nm filter before the detector. Experiments were performed with the incoming polarisation in the horizontal direction of the shown images and no analyser was employed.

Berreman calculus

We computed the transmission spectra and colour rendering using 'dtmm' software package, which uses the Berreman 4×4 matrix method to calculate the transmission and reflection spectra. We first calculated the transmission spectra assuming standard daylight conditions using D65 standard illuminant. The calculated spectra were then converted first to XYZ colour space using CIE 1931 colour matching function. Next, we computed the linear RGB colour from XYZ colour space, as described in the sRGB standard IEC 61,966-2-1:1999. Finally, we (optionally) applied the sRGB transfer function (gamma curve) to obtain the final nonlinear RGB colour values suitable for display or print. In the absence of the sample and with uncrossed polarisers, the above-described procedure converts the input light source spectra to a neutral grey colour. Therefore, to match the experimentally obtained images with the simulations, we performed in-camera white balance correction to get a neutral grey colour of the microscope's light source. The white-balance correction performs matching of the camera's tri-stimulus values for a given light source to the ones obtained under daylight conditions, allowing us to have a good match between the simulated and experimentally obtained images.

Experiments done in the IPS cell were measured with a BFLY-U3-23S6C-C camera, with no gamma correction, and we left the data in the linear RGB colour space. According to the manufacturer's specifications, the camera's IR filter has a short-pass filter characteristic with a cut-off at 620 nm. Therefore, we simulated the IR filter's short-pass characteristics for these experiments by limiting the light source spectra to the specified cut-off wavelength. We did not apply gamma correction to

obtain results in Figure 11. Experiments done in planar cells were done with a Canon EOS100D camera, which uses an sRGB transfer function. Therefore, we applied the gamma curve to the simulated linear RGB data to obtain the resulting images in Figure 10 and SI.15.

Cross-Differential Dynamic Microscopy (c-DDM)

The Cross-Differential Dynamic Microscopy method was setup as extensively described in reference [20] by Arko and Petelin. The setup comprises an infinity-corrected microscope objective with a 20× magnification, a 20 mm focal length tube lens followed by a beam-splitter, and two identical cameras (Flir BFS-U3-04S2C-CS with 6.9 μm pixel size and 1/3 inch sensor). Translational and rotational mechanisms ensure precise alignment of their field of view, and we aligned the cameras using an alignment ruler. For illumination, we used the Koehler illumination setup using Thorlab's M565L3 mounted phosphor-converted LED with a nominal wavelength of 565 nm and a bandwidth of 100 nm. The LED was operated in a pulsed regime with a low duty cycle to prevent sample heating, driven with a current of 5 A. Cameras were triggered as described in reference [20] to acquire two different sets of images with varying times of acquisition. Camera exposure time was 60 μs, and we set the shortest time delay between two consecutive frames on cameras to 256 μs. The image sequence is then cross Fourier analysed as a function of time delay using an open-source package 'cddm' to obtain the normalised image cross-correlation function [21].

Similarly, to traditional dynamic light scattering experiments, c-DDM allows studying the orientational fluctuations of the director field. LCs are characterised by two fundamental modes, the splay-bend ($\beta = 1$) and the twist-bend ($\beta = 2$) modes with relaxation rates:

$$\frac{1}{\tau_\beta} = \frac{K_\beta q_\perp^2 + K_3 q_\parallel^2}{\eta_\beta(q)} \tag{1}$$

where $q_\parallel$ and $q_\perp$ are the components of the wave vector parallel and perpendicular to the director, η_β are the viscosity coefficients and K_i are the splay ($i = 1$), twist ($i = 2$) and bend ($i = 3$) elastic constants. In the experiments, we aligned the polariser and analyser with the planar-aligned director. For this geometry, one can show that if the wavevector q of the analysis is along the director, then the obtained relaxation rate in the N phase corresponds to a pure bend-mode relaxation [22]. If the wave vector is orthogonal, the relaxation rate is that of a pure twist mode [23].

Quantum chemical calculations

Computational chemistry was performed in Gaussian G09 rev D01 [24] on the ARC3 machine at the University of Leeds. Calculations utilised the M06-HF hybrid DFT functional [25] with additional D3 dispersion correction [26] and the aug-cc-pVTZ basis set [27]. The keywords Integral = UltraFine and SCF (max-cycles = 1024) were used to ensure convergence, while a frequency calculation was used to confirm the absence of imaginary frequencies and so confirm the optimised geometries were true minima.

Results

Material

The structure of the liquid-crystalline material RM734 (4-((4-nitrophenoxy)carbonyl)phenyl-2,4-dimethoxy-benzoate) and the phase sequence are presented in Figure 1(a). On heating, the crystalline phase melts directly into the nematic phase at 139.8°C and transforms into the isotropic liquid phase at 187.9°C. On cooling, RM734 exhibits the isotropic (I) to nematic (N) phase transition followed by nematic to ferroelectric nematic (N_S) transition at 132.7°C, which crystallises around 90°C, temperature which can vary depending on the cooling rate. The synthesis of RM734 is described in reference [10]. RM734 has a very large dipole moment (~11.4 D) as calculated at the M06HF-D3/aug-cc-pVTZ level of DFT, at an angle of 18.3° with respect to the molecular axis and is therefore mainly longitudinal [28]. Figure 1(b) shows the molecular dipole moment (red arrow) and the polarisability tensor (green arrows and ellipsoid) as calculated at the M06HF-D3/aug-cc-pVTZ level of DFT [28]. Whereas the molecular dipole moment forms an angle with respect to the molecular axis, the long axis of polarisability tensor is mostly defined by it.

The formation of domains in the N_S phase was explored in commercial EHC cells of different thicknesses (KSRP D-type of 5, 8, and 25 μm) and with planar aligning layer (aligning agent polyimide LX-1400 from Hitachi-Kasei and antiparallel rubbing). Response to applied electric fields was studied in commercial in-plane switching (IPS) LC cells purchased from Instec, with an electrode width and gap between electrodes of 15 μm and a cell thickness of 9 μm, and with planar alignment parallel to the electrodes (aligning agent KPI-300B, antiparallel rubbing). The IPS operation mode is illustrated in Figure 5(b). All such measurements were performed after cooling from the N phase. Additionally, N–N_S transition was also inspected in Instec IPS cells, equivalent to the former, but with the planar rubbing

perpendicular to the electrodes (same aligning agent and antiparallel rubbing).

N–N_S transition and domains

Regardless of the cell thickness, on cooling from the N phase (Figure 2(a)), the N–N_S transition is characterised by the observation, just above the transition, of initial freezing of the characteristic nematic flickering (director fluctuations) followed by strong fluctuations destabilising the homogeneous orientation of **n**, characterised by a striped texture (Figure 2(b)). As shown in reference [8] and here below, such stripes show a strong alternating SHG signal. On further cooling, a homogeneous texture is restored together with the flickering (Figure 2(b)) and afterwards a bright line front, usually starting on defect points, travels across the sample (Figure 2(c)). When two of these fronts come together, they either annihilate or, as in the case shown in Video 1 of SI, result in a domain wall (Figure 2(d)). Such walls, which are 'soft', usually reposition over time and deform under the application of electric fields, as will be shown below. Interestingly, when the wall travels parallel to the rubbing direction, it exhibits a strong tendency to show a sierra-shape configuration, with the

walls at angles between 50 and 70 degrees from the rubbing direction (Figure 2). When directed perpendicular to the rubbing direction, they slightly bend but run over long distances without drastic deformations. When observed with the cell's rubbing direction along the polarisers, the N_S phase before the wall propagation shows very good extinction (Figure 2(e)). However, after wall propagation dark extinction is lost for thin cells. Here, it should be mentioned that the final state and homogeneity of the sample depends strongly on the used LC cell. In EHC planar cells clean propagation of the wall leads to very large domains spanning up to several millimetres, sometimes even covering almost the full cell. Same behaviour is found for cells with smaller (5.4 μm) or larger (22 μm) thickness (Figure SI.1)

In either standard or IPS Instec cells, which use a different aligning agent to the EHC cells, in some areas some 'lens-structures' develop before the front propagation (Figure SI.2 and SI.Video 2). Such structures can be small, like reported in reference [13], or quite large as we usually found in some areas of IPS cells (up to several hundreds of μm). When the final structural relaxation propagates through the cell, the characteristic front does not travel through these structures, but the wall divides
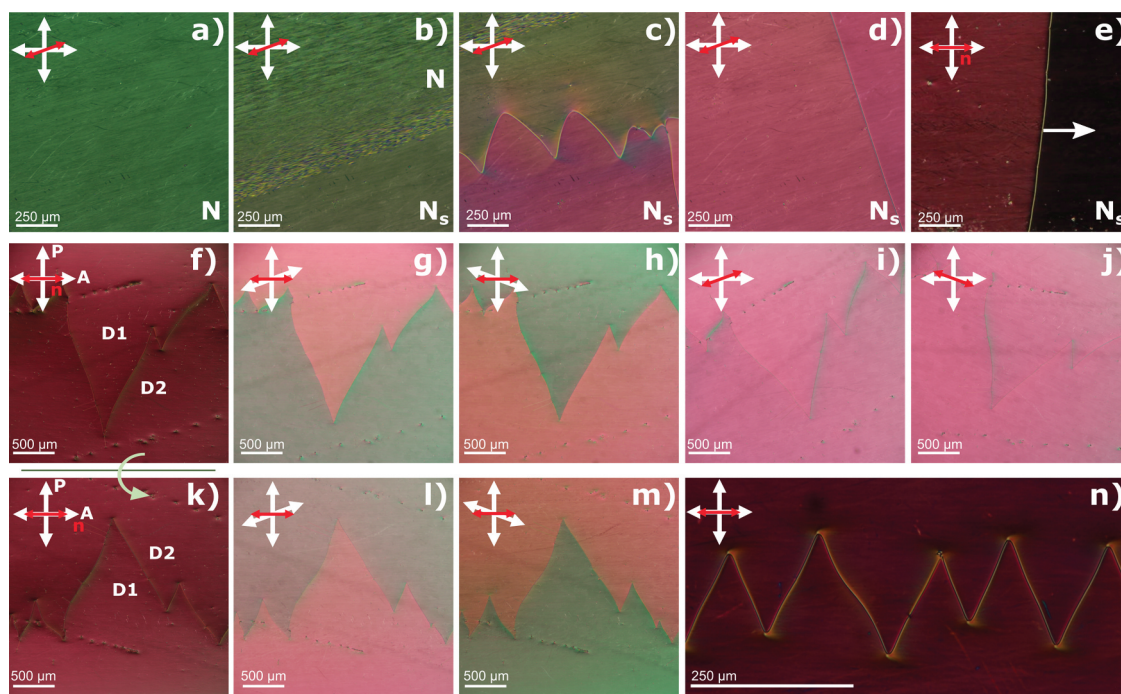

Figure 2. (Colour online) N–N_S transition and mm-size domains (a–e) Snapshots across the N–N_S transition. From left to right: (a) uniform N phase, (b) destabilisation of the homogeneous **n** orientation characterised by a stripped texture, (c) propagation of a π wall and (d) final N_S texture. (e) π-wall propagation for the sample in the extinction position. (f) Texture of the N_S phase of RM734 under crossed polarisers in extinction position and (g–h) by uncrossing the analyser by 20° clockwise and anticlockwise, indicating domains of opposite handedness separated by 'soft' walls. (i–j) Rotation of the sample between crossed polariser's reveals symmetric behaviour for rotations of 20 degrees clock and anticlockwise. (k–m) Flipping the sample upside-down around the cell rubbing direction evidences the same optical activity for domains D1 and D2 under uncrossing the analyser. (n) Typical sierra-shape configuration of the 'soft' walls separating domains. Cell thickness is 8.3 μm for images (a–m), 5.4 μm for (n) and red allow indicates the rubbing direction.

and surrounds them giving rise to a bright domain wall which is pinned to the surface (Figure SI.2 for localised structures and SI.Video 2 for larger areas). Such walls, which are 'hard', stay fixed in place and do not deform under electric fields. They can be localised or cover the whole cell and can be found both, in freshly filled cells (Figure 3(a)), indicating a precondition of the cell, or in cells where they were initially absent after application of electric fields. In either case, heating the sample back to the N phase melts them but on cooling back to the N_S phase the 'hard' walls tend to appear in the same areas, indicating a strong surface memory effect.

Further information can be obtained from POM observations. Focusing attention on those domains divided by 'soft' walls, it can be seen that such domains do not show extinction when aligning the rubbing direction with the analyser as shown in Figure 2 (e) and (f). When uncrossing of the analyser by a small angle (20°) in opposite directions, opposite optical activity is revealed suggesting the presence of a twisted structure with opposite handedness (see Figure 2(g,h)). Rotation of the sample anticlockwise and clockwise with respect to the crossed polarisers reveals no textural differences between both domains in this geometry Figure 2(i,j). Up-down rotation of the sample around the cell´s rubbing directions (Figure 2(k-m)) shows that each domain shows the same optical activity on uncrossing the analyser in the same direction, indicating the presence of just one twist handedness through the domain. Same studies on those domains enclosed by 'hard' walls (Figure 3), reveal that uncrossing the analyser results in opposite optical behaviour within each domain for opposite uncrossing but also opposite behaviour to that of the soft domain it is embedded in (Figure 3(c–d)). However, rotation of the sample clockwise or anticlockwise shows opposite colour texture (Figure 3(e–f)), evidencing that the twist structure inside these domains should be different than that of the predominant ones.

Finally, we checked the behaviour of the N–N_S transition in IPS cells equivalent to the previous ones, but, in which the aligning rubbing direction (same aligning agent and antiparallel rubbing, see Materials) is directed perpendicularly to the electrodes. Interestingly, the N–N_S transition manifests differently in this case. Destabilisation of the homogeneous nematic director and the striped texture are followed in this case by the formation of large elongated structures, covering the whole area of the cell, which flow, join annihilate and slowly stabilise into smaller domains embedded in a larger domain (Figure SI. 3 and SI. Video 3). Structural relaxation as observed in the previous cells (Figure 2(d,e)) does not occur. In the present case, sudden changes in the walls separating the domains can be observed, propagating from one end to the other (SI. Video 3). The final texture appears uniform with embedded domains. Aligning the cell rubbing direction with the crossed polarisers reveals a much better extinction than in the previous cells (Figure SI.4 (a)). When uncrossing polarisers in extinction position and rotating the sample between crossed polarisers symmetric optical behaviour can be observed, changing inside the smaller domains, but also varying in the matrix domain at long distances (Figure SI.4(b–e)). This indicates that the director structure might not be as uniform as would be assumed at first sight.

In this contribution, due to their prevalence in the different observed cells, we mainly focus on the electro-optic behaviour of the complementary domains divided by the soft walls described in this section (Figure 2).

Application of out of plane fields

As mentioned previously, when cooling from the N phase into the N_S, very large domains of several millimetres are obtained (Figures 2 and 4 (a–c)). Application of out of plane electric fields shows a variety of behaviours, whose in-depth analysis is not the scope of this paper. There are however several features that are worth mentioning. In EHC cells (5.4 μm), under application of low frequency (1 Hz) square-wave voltages and at low amplitudes (up to $V_p = 1$ V) the optical texture remains unchanged, walls slightly deform and domains blink in a non-uniform manner, strongly depending on surface defects. For higher voltages ($V_p = 1.5$ V, see Figure 4(d)), the domain walls start to strongly deform, with those running parallel to the rubbing direction adopting the sierra-shape configuration mentioned before (see area surrounded by the ellipsoid in Figure 4(d)), while those running perpendicularly to the rubbing direction retaining their shape. In some spots in the middle of domains where prior to field application no defect or dust was present, line defects initially grow which gradually 'open' giving rise to new domains. Figure 4(e,f) shows the same sample area as in Figure 4(a), after the field was switched off, evidencing that the initially large domains have broken down into smaller domains by the emergence of new ones, but with similar optical activity as the originating ones. New domain walls formed in this way show a stronger tendency for the sierra-shape configuration, with much shorter periodicity. The application now of square-wave of low amplitudes and different offsets reveals a second interesting finding observed repeatedly in these domains. When voltage is alternated between $-V_p$ and V_p domains remain 'unchanged' just blinking as described before (Figure SI.5(a) and SI.
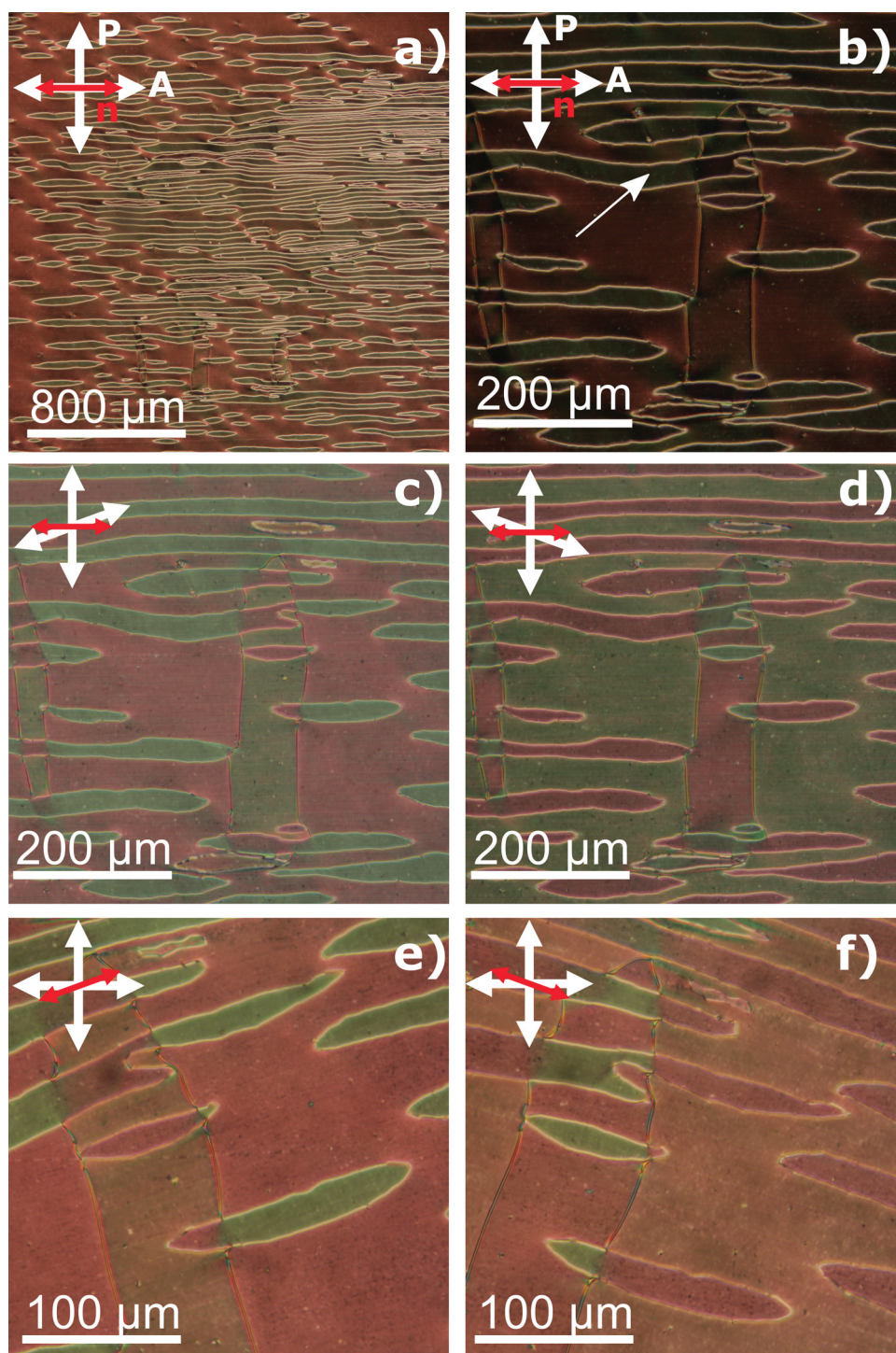
Figure 3. (Colour online) 'Hard' domains. Observation of domains delimited by 'hard' walls. While isolated 'hard' domains can be found, it is common to find large areas covered by them (a). Example pointed by white arrow image (b) in a background of π-twist domains. (b) Extinction, (c,d) uncrossing analyser in opposite directions and (e,f) rotating the sample with respect to extinction position between crossed polarisers in opposite directions. Areas within the hard domains show contrasting behaviour for opposite rotation. It is interesting to note that when one of such domains 'crosses' a 2π- wall the behaviour is reversed.
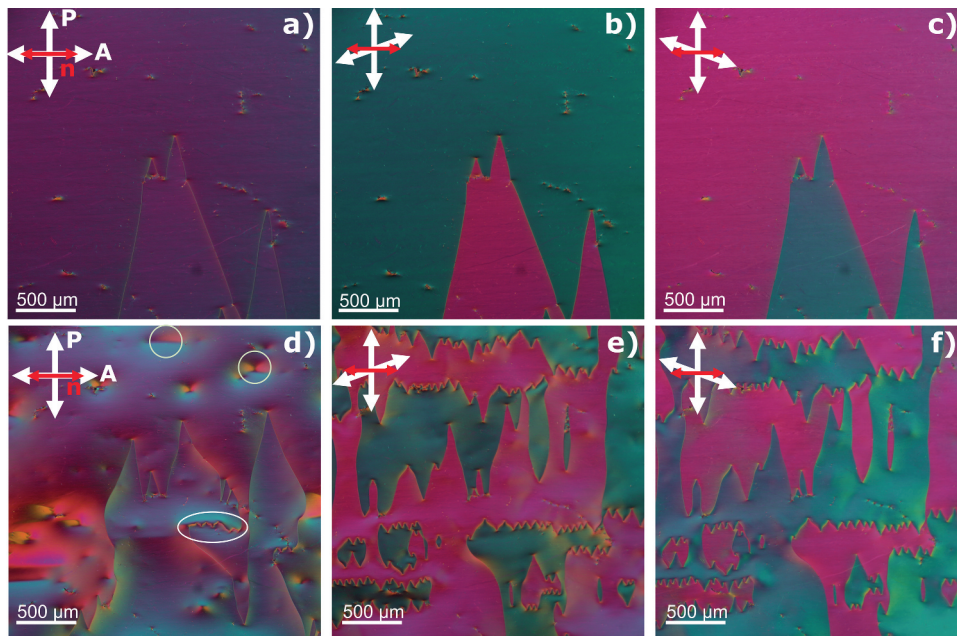
Figure 4. (Colour online) Domain division/creation by application of out of plane fields, in an EHC 5.4 μm cell at T = 120°C. Before application of field between crossed polarisers (a), and with analyser uncrossed (b,c). (d) Texture observed during the application of 1 Hz square-wave field of V_p = 1.5 V. (e,f) Final state of the sample after the field is switched off.

Video.4). If voltage switches from 0 to $2V_p$ one of the domains (D1) starts to progressively shrink (or equivalently domain D2 starts to grow), showing that such field polarity is not favourable for this domain (Figure SI.5(b) and SI.Video.4). If the field is switch back to alternate between $- V_p$ and V_p domain walls stop and stay in place. Finally, if now the voltage switches from $- 2V_p$ to 0, those domains previously shrinking, start to gradually grow again (Figure SI.5(c) and SI.Video.4) indicating that in this case, the field polarity is favourable within the domain.

In-plane electro-optic behaviour

Pulses

We investigated the electro-optic response to in-plane electric fields of the N_S phase at a temperature well below the transition (120°C°, T_{N-Ns}-T = 12), by means of POM as described in the Methods section. To minimise the effect of mobile charges, we applied a voltage pulse sequence (see Figure 5(c)) consisting of two opposite 50 ms pulses separated by 450 ms and with a repetition rate of 1 second, with peak voltages between V_p = 30 mV and V_p = 1.2 V (E fields between 2 V/mm and 80 V/mm in the plane between the electrodes). Experiments were performed for three different angles (ϕ = 0°, 20° and 45°) between the rubbing directions and the crossed polarisers and the sequence corresponding to one second period was

then reconstructed prior analysis (SI.Video.5). For the rubbing direction along the crossed polarisers, the typical electro-optic response is given in Figure 5(a), corresponding to snapshots for three different values, but at the same polarity, of the applied electric field for two domains separated by a 'soft wall'. Similarly, in Figure 5(d), the optical response at different times of the pulse sequence is shown for a given field. There are two significant characteristics to be noted. Firstly, the optical response to the test fields inside a given domain is non-symmetric with respect to the field direction. Secondly, the optical response is equivalent, but opposite with respect to the field polarity at both sides of the 'soft wall' dividing the domains. This is clearly shown in the mean intensity profile plot in Figure 5(e) and the time dependence mean intensity plots shown in Figure 6(a) and Figure SI.6 for different areas in the texture corresponding to different field directions, in-plane (between electrodes) and out of plane (above electrodes). Inside a given domain, for voltages below V_p = 600 mV, the transmitted intensity between crossed polarisers increases for a given field direction during the pulse duration, while decreases when the field is in the opposite direction as shown in Figure 6(a). Given the alternating field distribution of the IPS cells as sketched in Figure 5(b), the described behaviour results in alternating switching inside a domain. The next domain, on the other hand, shows the same response
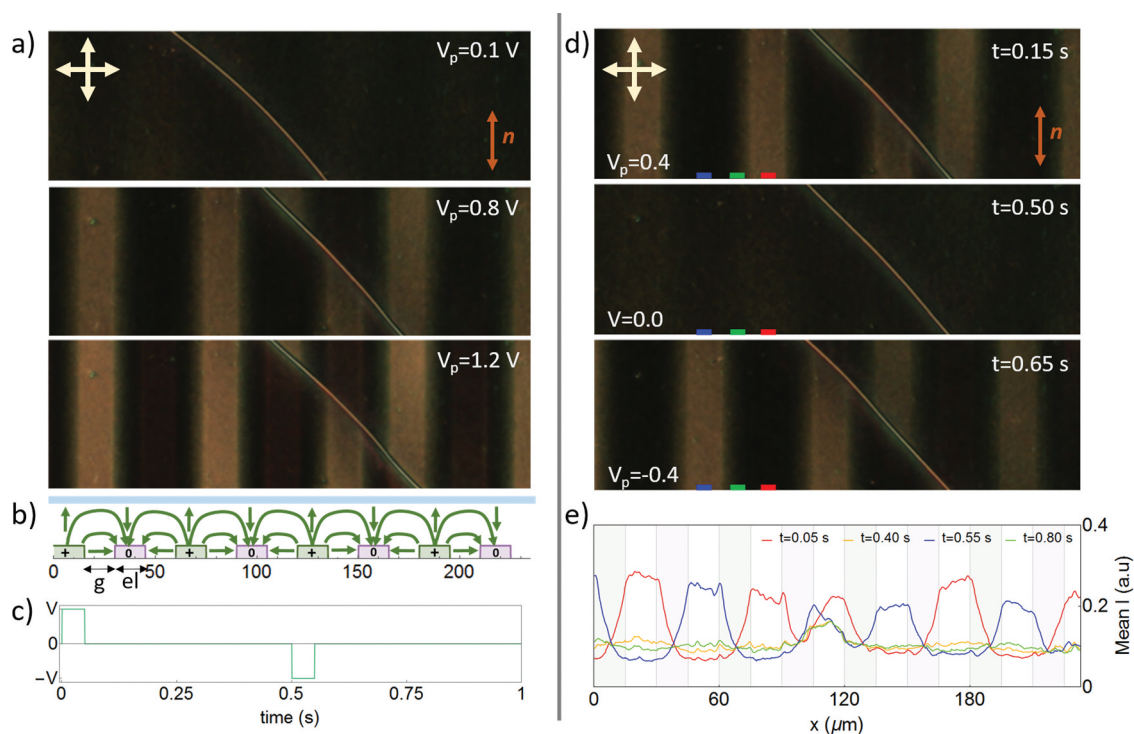
Figure 5. (Colour online) (a) Polarising optical microscopy (POM) images showing in-plane switching of the N_S phase at 120°C ($T_{N-Ns}-T = 12$) for two opposite domains separated by a domain wall at different V_p. (b) Schematic of the corresponding section of the cell geometry, where green arrow represents the electric field vector for a given polarity of the field. Both, the width of the electrode (e) and of the gap (g), corresponds to 15 µm. (c) Applied pulse sequence, with two opposite pulses of 50 ms, separated by 0.5 s. (d) POM snapshots of the switching sequence at three different times corresponding to the pulses peaks and 0 field. (e) Intensity profile over the direction perpendicular to the electrodes for the snapshots in (d). Time has been shifted 0.1 s for correspondence with Figure 6 and better visualisation.

but reversed with respect to the voltage peak sign (Figure 5(d,e), Figure 6(a) and Figure SI.6). When varying the field amplitude, for a given gap within electrodes, transmitted intensity increases steadily for one field direction, while decreases, reaches a minimum and starts increasing, for the opposite field direction (Figure 6(b)) and Figure SI.6).

In the case of the electro-optic response recorded for the rubbing direction at 20° with respect to the crossed polarisers, results are comparable (Figure SI.7). Transmitted intensity at zero field (I_0) increases as expected from $I = I_\phi \sin^2\phi \sin^2(\pi\Delta nd/\lambda)$. Normalised intensities over reorientation are qualitatively similar to what is observed for $\phi = 0°$, while the larger I_0 value results in lower contrast and the minimum on the normalised mean intensity slightly shifts towards lower fields. However, when we observe the electro-optic response at $\phi = 45°$ (Figure SI.8), the difference between both field directions in the same electrode gap becomes nearly indistinguishable. Additionally, the minimum of the transmitted intensity shifts nearly to zero field, but of the opposite sign from the scenario for

$\phi = 0°$ and $\phi = 20°$ (Figure 7). Finally, less noticeable changes in the transmitted intensity can be detected on top of the electrodes; however, the non-uniform field profile together with the penetration of the signal coming from the large reorientation in-between the electrodes restricts the analysis. We estimated optical raise and relaxation times from the pulse experiments at $\phi = 0°$ and three different applied pulse voltages ($V_p = 0.6$ V, 0.8 V and 1.2 V, see for example Figure SI. 9), from the usual definitions optical transmittance change from 90% to 10%. Obtained values (see SI) show that the rise time almost remains unchanged, with a slight increase for increasing fields. Switching behaviour critically depends on the inner field that at the same time critically depends on the inhomogeneous structure of the polarisation and charge distribution.

Square-wave

Unfortunately, due to the limiting scanning frequencies for the SHG-experiment detailed below in next section, short pulse sequences can not be
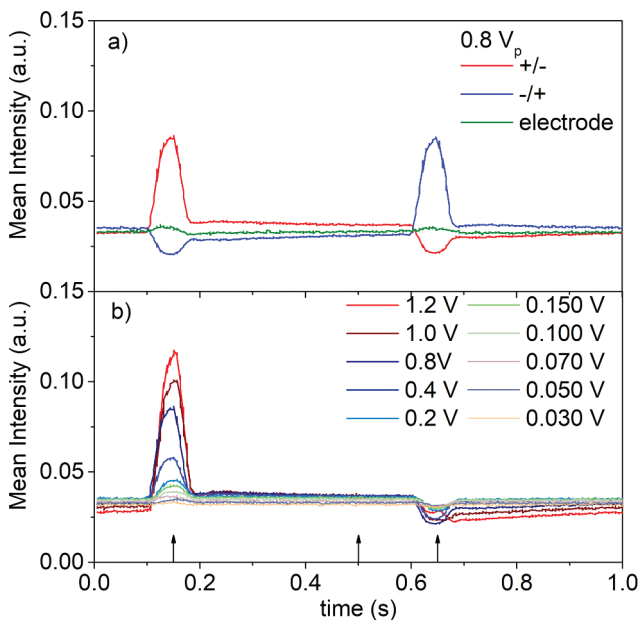
Figure 6. (Colour online) Time dependence over the switching cycle of the transmitted intensity for the cell oriented with the rubbing direction along the analyser in the N_S phase at 120°C ($T_{N\text{-}Ns} = 12$). (a) For a given V_p for the three areas marked in Figure 2 within the same domain: red (one field direction), blue (opposite field direction) and green (over the electrode). (b) For the area marked as red at different field strengths. Time has been shifted 0.1 s for better visualisation.
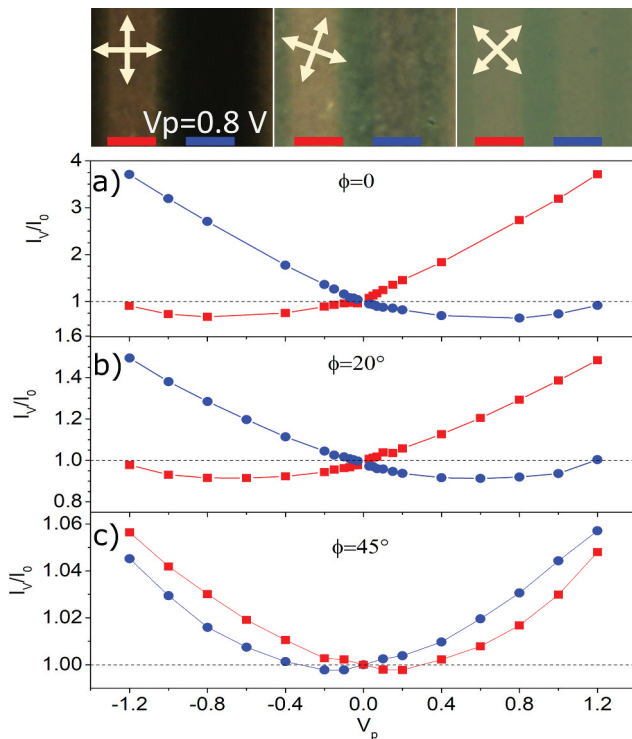

Figure 7. (Colour online) Normalised mean intensity (I_V/I_0) over reorientation for two areas within a domain corresponding to opposite fields, marked by the red and blue bar in the top POM images. For rubbing direction at (a) 0°, (b) 20° and (c) 45° with respect to the crossed polarisers.

employed and the use of square-wave voltages profiles is necessary. Thus, for comparison with the electro-SHG experiments, the electro-optic response was also studied under the application of square-wave 1 Hz driving fields, for $\phi = 0°$ (Figure 8 and Figure SI.10). Results are qualitatively similar to those obtained with the pulse sequence, where, for a given domain, one field direction results in the increase of transmitted intensity while the opposite field direction leads to a decrease, clearly observed in Figure 8(b). The switching, though, is bimodal, with a very fast initial response (~ms) to the field sign reversal followed by a much slower process. Indeed the transmitted signal does not appear saturated before reaching the field reversal point. Comparison of the normalised mean intensity
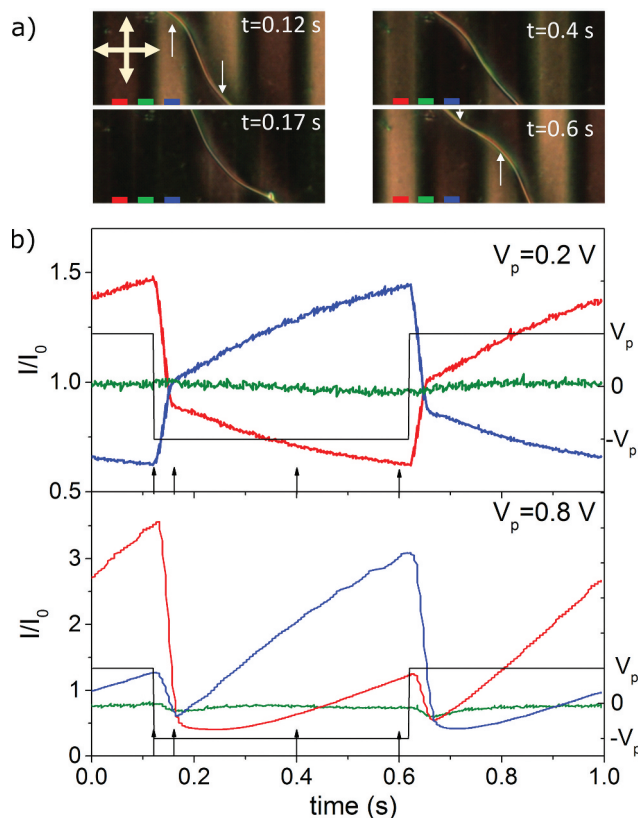

Figure 8. (Colour online) (a) POM snapshots of the electro-optic response to the application of a square-wave (1 Hz, $V_p = 0.8$ V) at different times of the switching cycle for the rubbing direction of the sample cell at 0° with respect to the crossed polarisers. White arrows point towards the bend direction of the domain 'soft' wall, indicating that the area with larger transmitted intensity under field expands, while that with lower transmitted intensity contracts. (b) Time dependence of the main intensity during a switching cycle for those areas marked in (a): red (one field direction), blue (opposite field direction) and green (on top of the electrode) for peak voltages of $V_p = 0.2$ V and $V_p = 0.8$ V. Black arrows correspond to the times of the snapshots in (a). Right axis shows the phase of the applied square-wave form.
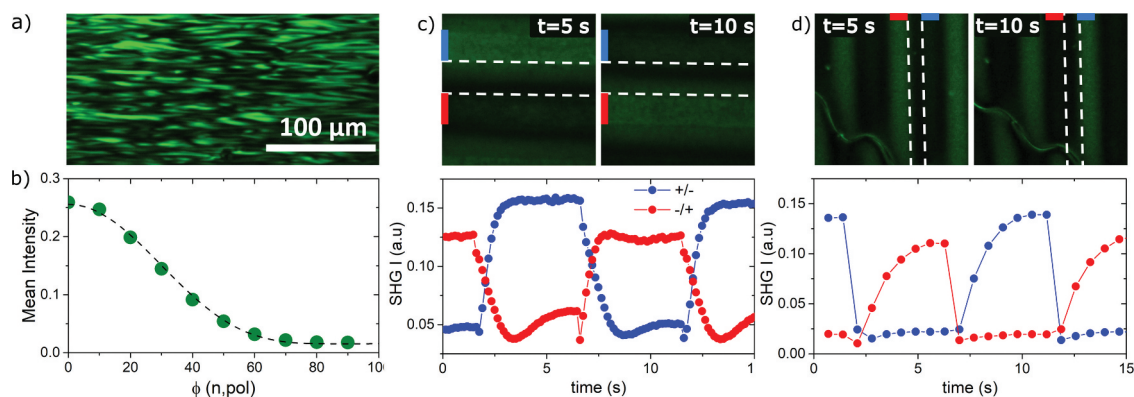
Figure 9. (Colour online) Second harmonic generation (SHG) (a) Snapshot at the transition showing a periodic pattern with a periodicity of: 10 μm. (b) Angle dependence of SHG signal, where ϕ is the angle between the incoming polarisation and rubbing direction. Dashed line corresponds to the fit $\propto cos^4\phi$ (c) SHG images of the switching response for a square wave of 0.1 Hz and $V_p = 0.75$ V, when the initial **n** direction is parallel to the incoming light polarisation. Bottom plot shows the time dependence of normalised SHG intensity during the switching. (d) SHG images when the initial **n** direction is perpendicular to the incoming light polarisation. Bottom plot shows the time dependence of SHG intensity during the switching.

I_V/I_0 at different times with that obtained from the application of short pulses (Figure SI.11) shows that in experiments for which short pulses were employed, reorientation is almost, although not fully, completed during the short pulse. Due to the time dependent square voltage profile, where $-V_p$ and V_p are applied for sufficiently long times, mobile charges, e.g. ionic impurities in the LC, have time to redistribute, which results in screening effects on the applied fields and of the polarisation charges. Such effects lead to longer equilibration times for the electro-optic response. This shows that short pulse sequences are better for probing the equilibrium structure as in the case of square-wave, ion dynamics would need to be taken into account.

Application of square-wave also revealed a limiting voltage above which no equilibrium structure is achieved. At $V_p = 1.4$ V structure starts to destabilise, as seen in Figure SI.12, eventually leading to the onsite creation of new walls, domains and flow. Such studies although interesting, are out of the scope of this paper.

Second harmonic generation

To gain insight into the reorientation of the polarisation direction under the application of in-plane perpendicular fields, we performed SHG imaging in the same IPS cells (see Methods). Measurements were performed with polarised incoming laser beam and no analyser. On cooling from the N phase, as already reported [8], a periodic stripped texture can be clearly observed by SHG imaging (Figure 9(a)), with a periodicity of around 10 μm (incoming polarisation parallel to rubbing

direction). On further cooling, the SHG texture becomes uniform and darkens after the propagation of the structure relaxation lines described previously (transition sequence shown in Figure SI.14). The dependence of the transmitted SHG intensity on the angle between rubbing direction and incoming polarisation is shown in Figure 9(b) for a temperature after the structural relaxation. The observed angular dependence follows the dependency $I_{2\omega} \propto cos^4\phi$, indicating that the main SHG activity arises for the polarisation of the pump laser along **n**.

Due to small scanning rate of the confocal microscope, IPS was studied for 0.1 Hz square pulses for voltages of $V_p = 0.75$ V. The scanning rate of the confocal microscope was set to 1800 Hz resulting in an acquisition rate of 6.8 frames per second. Comparison of the wall deformation under fields allows correlating SHG results to those obtained by POM (Figure SI.14). When incoming polarisation is parallel to rubbing, for the same polarity at which POM results show a decrease in the transmission intensity (for example red area in Figure 8 at 0.5 seconds) the SHG signal initially significantly drops and then equilibrates to larger value, although lower than in the absence of electric field. Observed equilibration times are large, in the range of seconds. For the opposite polarity (that at which transmitted intensity strongly increases in POM), SHG signal is larger and of the order of that observed without electric field. When incoming polarisation is perpendicular to rubbing (Figure 9(d)), scan rate 700 Hz and 1.4 fps due to the larger scanned area), the SHG signal is very weak when the field is off in agreement with Figure 9(b). When applying the field, SHG signal increases strongly for the field polarity at which POM

shows larger transmission (for example red area in Figure 8 at 0.1 s, compare with wall deformation in Figure 9(d)) and almost no change can be detected for that polarity at which the POM transmission changes little.

Discussion

Comparison of the textural features observed in different types of commercial cells shows the strong effect that surfaces have on the final structure of the N_S phase in confinement. While in those planar EHC cells with anti-parallel rubbing (treated with polyimide LX-1400 from Hitachi-Kasei), only one type of domain has been observed, separated by 'soft' walls, observations in planar Instec cells (KPI-300B) also with antiparallel rubbing have shown a broader hierarchy of structures. For the latter, even when comparing cells from the same batch (for example Instec IPS cells with rubbing antiparallel to the electrodes) big differences have been observed from cell to cell. For some of these cells, only big domains separated by 'soft' walls are present while for the others the whole area is covered by smaller domains divided with 'hard' walls embedded in large domains of the previous type. Interestingly, as also observed in Instec IPS cells, although aligning agent and the antiparallel type of rubbing are the same, the N–N_S transition manifest very differently for cells with the rubbing parallel or perpendicular to the

electrodes. The observed textural features depend not only on the surface properties, but also on the history of the sample/surface. It has been observed that the application of electric fields can result into the nucleation of 'hard' wall-surrounded domains in areas where they were previously absent. Heating back to the N phase and cooling down into the N_S reveals that those 'hard' walls are triggered by the local characteristic of the surface, as they will reappear in the same areas. These observations indicate, not only that experimental observations for N_S phase have to be done by carefully controlling the confining media surfaces, but, most importantly, that the control of confining surfaces can be used to manipulate the macroscopic structure of the sample.

Optical observations summarised in Figure 2 demonstrate that those domains predominantly found in our experiments exhibit twist deformations with opposite handedness. Furthermore, those observations confined in Figure 3, Figure SI 3 and SI 4, further reveal the strong effect of surfaces on the director structure as evidenced by the optical behaviour. To gain insight into the structural twist features we performed Berreman calculations to describe the expected optical behaviour for different twist structures and experimental geometries. Taking into account a cell thickness of 8.8 μm and $\Delta n = 0.24$, we investigated the resulting transmitted spectra for the three simple twist geometries for the same conditions as experimentally shown in
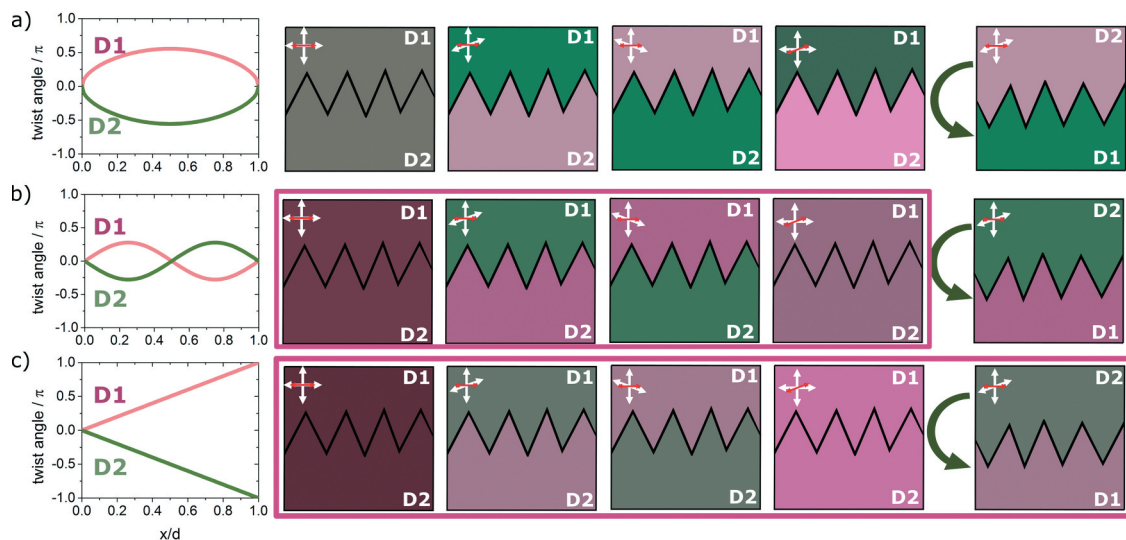

Figure 10. (Colour online) Berreman calculus for different twist structures. (a) Domains with opposite handedness single twist, (b) Domains with opposite handedness double twist and (c) domains with opposite handedness π-twist. Left plots show the twist structure used in the calculations, while in the right results are shown for (from left to right) domains in extinction position, uncrossing analyser in one direction, uncrossing analyser in the opposite direction, rotating the sample in one direction and finally, upside-down flipping of the sample around the cell rubbing direction. Enclosed in rectangles are those results that match with the experimentally observed behaviour shown in Figure 2 of the main manuscript.

Figure 2. Given the presence of a structural π-relaxation in the predominant domains (Figure 2) and the absence of it in other cases (Figure SI 2,3 and 4), twist structures with and without π reversal in the surface were tested, i.e simple twist (Figure 10(a)), double twist (Figure 10(b)) and full-pi twist deformation (Figure 10(c)). We should note here that the simple twist and double twist geometries would lack of physical meaning in the case of a uniform ferroelectric nematic phase, however, they have been included in the comparison for being the simplest twist geometries that account for some of the observed optical features as will be seen below. Due to their predominance in this study, we first focus on the mm-sized domains divided by 'soft' walls. Although the three twist structures can account for the optical symmetry revealed in this case under uncrossing the analyser, a simple lens-like twist (Figure 10(a)) fails to account for the optical degeneracy observed under sample rotation with respect to the crossed polarisers. Double twist (Figure 10(b)) and full-pi twist (Figure 10(c)) structure can explain such observations. However, for the double twist structure, calculations show that when flipping upside-down the sample around the cell rubbing direction and with the analyser slightly uncrossed, domain optical activity is expected to reverse (Figure 10(b)) which is not observed in the experiments. In short, only the full π-twist structure accounts for all the observations summarised in Figure 2 for the considered type of domains. Direct comparison of the POM observations of Figure 2 and Berreman calculus of Figure 10, together with the addition of a 530 nm lambda plate can be found in Figure SI. 15. Thus, left handed and right handed twist domains, are separated by 'soft' walls, topologically 2π disclination lines, which are not pinned to the surface and can move. And, as has been shown, they easily deform under the application of small electric fields. This is in agreement with those results presented in reference [29], in which the appearance of the twist across the cell is attributed to the antiparallel unidirectional rubbing resulting in opposite in-plane polar anchoring in both surfaces. Charged surfaces result in a small electric field pointing out of the surface plane, which can force the sample polarisation to orient out of the plane. In the presence of a cell pretilt, as is the case for antiparallel rubbing, pretilt and out of plane electric field will result into opposite orientational effect for the polarisation at the cell surfaces, which can be the reason behind the formation of a full π-twist structure across the cell [29]. Probably it is interesting to recall at this point, the very different equilibrium states obtained for the N_S phase in the Instec IPS cells (same aligning agent and anti-parallel rubbing for both surfaces, i.e. pretilt) for the rubbing being parallel to be perpendicular to the electrodes. In the latter, no twist structural relaxation is observed resembling more the observations discussed for bidirectional rubbing with no pretilt [29].

Additionally, results shown in Figure 10 can be related to the textural observations for those domains enclosed by the hard domains. It is worth recalling, that as shown in Figure SI.2, the twist structural relaxation characterised by the full π-twist propagation does not occur in these domains. In this case, rotation of the sample in opposite directions reveals different colour texture, indicating that the twist structure is different than the full π-twist. Comparison of experimental observations (Figure 3) and the calculations (Figure 10) shows that from the considered simple twist structures, the only one that accounts for the first is the simple twist structure. As mentioned before, such domains grow in areas where before the structural relaxation a lens-shape structure is observed, similar to those reported in reference [29] for surfaces with bidirectional rubbing. In Figure 3 it can be seen that, when one of these domains crosses several larger π-twist domains, texture colour alternates on sample rotation when going from one surrounding π-twist domain to the adjacent, indicating that handedness changes across the domain without giving rise to a wall (Figure 3(e–f)). Additionally, when applying perpendicular in-plane fields, these domains show larger/smaller transmitted intensity for the field polarity at which the π-twist domain in which they are embedded shows larger/smaller transmission (Figure SI.13). These two observations together suggest that the simple twist structure is determined by the π-twist domain in which it is embedded and the position of the 'hard' domain wall, which is pinned at one of the surfaces and is separating the regions having opposite polarisation direction (Figure SI. 16). It is important to recall here that such simple twist structure is the simplest of the possible structures that account for the optical behaviour, and does not indeed need to be the real structure.

Returning to observations for IPS cells with rubbing perpendicular to the electrodes (Figure SI. 3, Figure SI. 4 and SI. Video 3), comparison with Figure 10 would suggest the presence of a simple twist structure in these domains. Although weak, differences can be observed when uncrossing polarisers or rotating the sample, suggesting that the structure is not uniform and that the direction of the twist

can change over long distances. Application of small voltages (Figure SI.4(f), in this case, field directed along the rubbing direction) shows that one of the field polarities is favourable for the domain polarisation resulting in little reorientation, while the other polarity provokes a large reorientation of the material. Additionally, Figure SI.4(f) evidences that the average polarisation direction of neighbouring domains lay in opposite directions.

We used the same formalism to calculate the normalised transmitted intensities under the applications of in-plane fields directed perpendicularly to the cell rubbing direction as analysed in the electro-optic experiments presented here. For that, the previous required step is the calculation of the director structure under the application of an in-plane electric field. We considered a simple model in which the field reorients the polarisation, which remains constant and parallel to the director. That being said, the application of an electric field will also increase the order of the dipoles and can also induce dipole moments, but such effects have not being taken into account for the shake of simplicity. In the absence of an applied field, the nematic director was considered to make a full uniform π-twist turn along the cell thickness. Equilibrium solutions under field where calculated as described in SI. Section I. considering a cell thickness of 9 μm and $\Delta n = 0.24$, calculated normalised intensities are shown in Figure 11 as a function of a normalised applied field (SI.Section I). Comparison with Figure 7 shows good agreement with experimental findings, where for a given field polarity normalised transmitted intensity linearly grows at small fields while decreases for the other polarity reaching a minimum at sample rotations of 0 and 20 degrees.
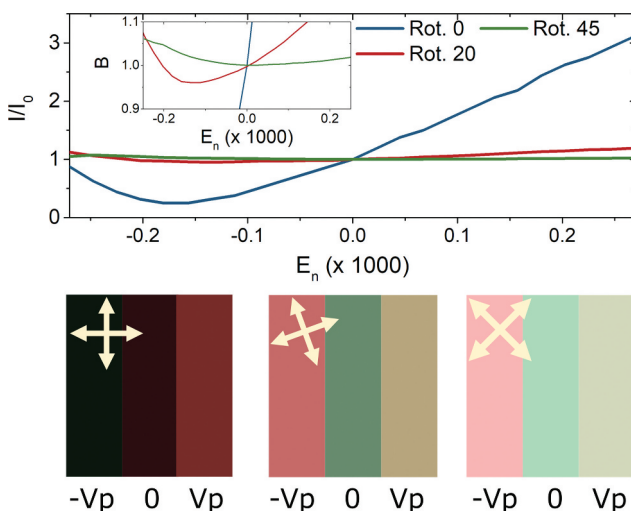

Figure 11. (Colour online) Top: Calculated normalised transmitted intensity as a function of the normalised electric field for the structure given in Figure 10c. Bottom: Example of calculated optical behaviour for $V_p = \pm 0.0024$.

Even in the case of the sample rotated at 45 degrees with respect to the crossed polarisers calculations are in very good agreement with experimental results. Calculations not only accurately reproduce the experimental trend but also the observed normalized transmitted intensity values. One should keep in mind, that calculations with a more 'complex' full π twist, as in more localised structure, show similar results than the continuous full π twist, both for the observed characteristics under no field and for the field dependence of the transmitted intensity. This suggests that continuous π-twist is only one of the possible structures and that distinguishing between them requires experimental evidence beyond optical observation. The same Berreman calculations could be performed for SHG observations, however, one should bear in mind that such analysis is more complicated as it strongly depends on the details of the structure. As shown in Figure 9(b), the main contribution to the SHG signal arises from the polarisation of the laser parallel to the cell rubbing direction. In theoretically calculating the SHG signal one should take into account the how well optical polarisation is guided inside the sample, interference effects of the SHG beam and the effects arising from the increase of the polarisation due to the application of electric fields. Although feasible, such calculations can lead to wrong conclusions if the primary requirement, the knowledge of the fine details of the structure, is missing.

To further characterise the structural twist we performed c-DDM (see Methods) measurements at 120°C in two adjacent domains as those shown in Figure 2 ($T_{N-Ns}-T = 12$). c-DDM is a method equivalent to dynamic light scattering (DLS) (Figure 12 and Figure SI.17), in which the orientational fluctuations of the director field are measured. The advantage of the c-DDM over the DLS is that in a single measurement the relaxation rates at many values and directions of wavevector is measured. In the case of a bulk nematic with a uniform director field, the eigenmodes of the fluctuations are plane waves ([30]) and the dispersion curve (i.e. dependence of the relaxation rates of fluctuations on the wave vector) has uniaxial symmetry (Figure 12(a–b)). If equilibrium director field is nonuniform (due to nonuniform ground state, boundaries, field or presence of defects), the director thermally fluctuates around the equilibrium. While it is not possible to deduce the equilibrium structure from the dispersion curve, the latter reflects the symmetry of the nonuniform structure. Here, we will only focus on the shape and the symmetry of the q-dependence of fluctuations, which reflects the underlying director structure. Deeper analysis and modelling of the results will be presented elsewhere. When the system is in the ordinary
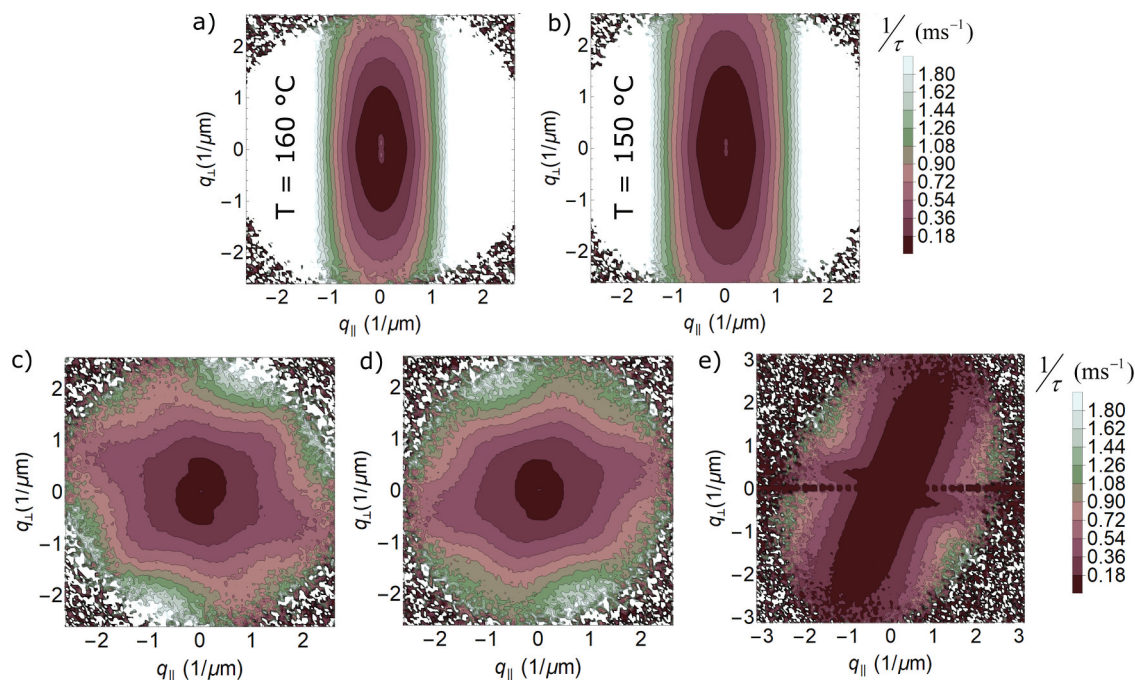
Figure 12. (Colour online) Cross-Differential dynamic microscopy examples in EE geometry. (a,b) Relaxation rates for RM734 at two temperatures of the N phase, 160°C and 150°C respectively. (c,d) q-dependence of relaxation rates for RM734 at 120°C in the N_S phase in two adjacent π-twist domains. (e) q-dependence of fluctuations for RM734 at 120°C in an Instec IPS 9 μm cell with the alignment layer rubbed perpendicularly to the electrodes, same cell as shown in POM experiments in Figure SI 3 and 4.

nematic phase, q-dependence surface plot is symmetric with respect to the rubbing, reflecting uniform orientation of the director, with faster increase of the relaxation rates with the wavevector parallel to **n** (see Figure 12(a,b)), due to faster bend fluctuations (Methods). When lowering the temperature in the N phase, slowing down of the fluctuations can be appreciated by comparison of q-dependence plots shown in Figure 12(a,b) [7]. In the case of a uniformly twisted structure, as for example appears in chiral nematic LC, the dispersion curve in a plane perpendicular to the pitch direction is circularly symmetric as shown in Figure SI.17(b–c) . In the N_S phase in the π-twist domains, the dispersion curves have star like shape (Figure 12(c,d)) with roughly hexagonal symmetry, indicating that the structure is not a uniform twist, but the director orientation seems to have three preferred in-plane orientations separated by localised twist deformation. In order to gain more information about the structure in the main domain observed for IPS cells with the rubbing perpendicular to the electrodes, we also perform c-DDM measurements in those. Comparison of the results shown in Figure 12(e) for the N_S phase at 120°C with those characteristic of the uniform N phase (Figure 12(a,b)) shows that the main orientation of the director is tilted in plane with respect to the cell rubbing direction. Such results are compatible with the presence of a simple twist structure as also suggested by the textural features (Figure SI. 4 and comparison with Figure 10).

The considered full π-twist can explain the optical observations and can be explained by the polar anchoring effects which will force polarisation in opposite directions at the surfaces of the cell. However, c-DDM results (Figure 12(c,d)) show that the twist structure in the absence of applied fields might be more complicated. Also, in the case of those cells studied in Figure SI.4, c-DDM shows a preferential twist angle away from the rubbing direction (Figure 12(e)). As pointed out before, simple twist geometries like that shown in Figure 10(a) are energetically unfavourable for uniform nematic phases. This indicates that the underlying structure can be more complicated. All these observations together open many questions. The appearance of twisted structures can be a consequence of the confinement and surface effects; however, it is also possible that the phase is intrinsically chiral. MD simulations showed that in the absence of the field the polarisation is parallel to the average orientation of the molecules [28]. However, the polar order of

molecular axis measured by $P_1 = \langle Cos(\theta) \rangle$, where θ is the angle between the director and the molecular axis is larger than the polar order calculated for the direction of the dipoles [28]. That the two order parameters are different is expected because the molecular long axis and the dipole are not parallel (Figure 1). While molecular axes are on average oriented along the director, the dipole moments are randomly oriented on a cone (Figure SI.18). It is expected that an electric field will increase the order parameter of the dipoles, one way this can happen is that the dipoles preferentially orient at an angle on the cone determined by the direction of the field (Figure SI.18), resulting in a structure that is biaxial. This situation is similar but not equivalent to the biaxial ferromagnetic phase [31]. Such polar biaxial phase is determined by two vector order parameters, and has therefore different symmetry than the non-polar biaxial phase that can be described by two tensors [32]. The response of the π-twist domains to an out-of-plane field (Figure 4, Figure SI.5 and SI.Video.4) depends on the handedness of the domain. At a field with a given sign, not only the domains with favourable handedness grow, but also new domains with this handedness emerge. One possible explanation of this behaviour is that the field through the induction of polar biaxial order indirectly also induces chirality, as polar biaxial phase can be chiral [33]. In such case in an unconstrained sample, the structure in the homogeneous external field could resemble polar heliconical structure (Figure SI. 19) in which the pitch depends on the magnitude of the field.

Due to the flexoelectric coupling, polar phase exhibits instability towards splay deformation [8], and, in the case, the director and polarisation are parallel, the splay deformation would cause the divergence of polarisation and consequently the depolarisation field. This field can either suppresse the splay, or as discussed above, can induce biaxial order combined with chirality. The latter would explain why the twist in π-twist domains could be localised, more in agreement of the c-DDM observations. The field at the surface causes twist in the regions at the surfaces, while inhomogeneous splay could cause it in the interior of the cell. Further testing of this hypothesis is above the scope of this paper.

All the experimental data reported here demonstrate a wide variety of behaviours. Confinement, surfaces, surface charges, thermal history, field or field application history are just an example of all the parameters which affect the final behaviour of the sample. These lead to a hierarchy of polar structures which can be easily switched by electric fields, clearly showing polar linear coupling. Understanding, control and exploitation of all these behaviours open an exciting path for the study of this new phase. For instance, SHG results show just part of the big application potential of this new ferroelectric nematic phase to be employed in photonic applications going beyond the classical LCs ones.

Acknowledgments

Disclosure statement

No potential conflict of interest was reported by the author(s).

Funding

ORCID

Nerea Sebastián ⓘD http://orcid.org/0000-0002-9156-1895
Richard J Mandle ⓘD http://orcid.org/0000-0001-9816-9661
Alexey Eremin ⓘD http://orcid.org/0000-0001-9743-6895
Alenka Mertelj ⓘD http://orcid.org/0000-0002-2766-9121

References

[1] Born M. Über anisotrope Flüssigkeiten. Versuch einer Theorie der flüssigen Kristalle und des elektrischen KERR-Effekts in Flüssigkeiten. Sitzungsber Preuss Akad Wiss. 1916;30:614.

[2] Palffy-Muhoray P, Lee MA, Petschek RG. Ferroelectric nematic liquid crystals: realizability and molecular constraints. Phys Rev Lett. 1988;60 (22):2303–2306.

[3] Bisi F, Sonnet AM, Virga EG. Steric effects in a mean-field model for polar nematic liquid crystals. Phys Rev E. 2010;82:041709.

[4] Dhakal S, Selinger JV. Statistical mechanics of splay flexoelectricity in nematic liquid crystals. Phys Rev E. 2010;81:031704.

[5] Berardi R, Ricci M, Zannoni C. Ferroelectric and structured phases from polar tapered mesogens. Ferroelectrics. 2004;309:3–13.

[6] De Gregorio P, Frezza E, Greco C, et al. Density functional theory of nematic elasticity: softening from the polar order. Soft Matter. 2016;12:5188–5198.

[7] Mertelj A, Cmok L, Sebastián N, et al. Splay nematic phase. Phys Rev X. 2018;8:041025.

[8] Sebastián N, Cmok L, Mandle RJ, et al. Ferroelectric-ferroelastic phase transition in a nematic liquid crystal. Phys Rev Lett. 2020;124:037801.

[9] Mandle RJ, Mertelj A. Orientational order in the splay nematic ground state. Phys Chem Chem Phys. 2019;21:18769–18772.

[10] Mandle RJ, Cowling SJ, Goodby JW. Rational design of rod-like liquid crystals exhibiting two nematic phases. Chem - Eur J. 2017;23:14554–14562.

[11] Mandle RJ, Cowling SJ, Goodby JW. A nematic to nematic transformation exhibited by a rod-like liquid crystal. Phys Chem Chem Phys. 2017;19:11429–11435.

[12] Connor PLM, Mandle RJ. Chemically induced splay nematic phase with micron scale periodicity. Soft Matter. 2020;16:324–329.

[13] Chen X, Korblova E, Dong D, et al. First-principles experimental demonstration of ferroelectricity in a thermotropic nematic liquid crystal: polar domains and striking electro-optics. Proc Natl Acad Sci. 2020;202002290. DOI:10.1073/pnas.2002290117

[14] Nishikawa H, Shiroshita K, Higuchi H, et al. A fluid liquid-crystal material with highly polar order. Adv Mater. 2017;29:1702354.

[15] Li J, Nishikawa H, Kougo J, et al. Development of ferroelectric nematic fluids with giant-ε dielectricity and nonlinear optical properties. Sci Adv. 2021;7:eabf5047.

[16] Saha R, Nepal P, Feng C, et al. Multiple ferroelectric nematic phases of a highly polar liquid crystal compound. ArXiv210406520 Cond-Mat [Internet]. 2021 [cited 2021 May 31]. Available from: http://arxiv.org/abs/2104.06520

[17] Čopič M, Mertelj A. Q-tensor model of twist-bend and splay nematic phases. Phys Rev E. 2020;101:022704.

[18] Shamid SM, Dhakal S, Selinger JV. Statistical mechanics of bend flexoelectricity and the twist-bend phase in bent-core liquid crystals. Phys Rev E. 2013;87:52503.

[19] Rosseto MP, Selinger JV. Theory of the splay nematic phase: single vs. double splay. ArXiv200312893 Cond-Mat [Internet]. 2020 [cited 2020 Apr 13]. Available from: http://arxiv.org/abs/2003.12893

[20] Arko M, Petelin A. Cross-differential dynamic microscopy. Soft Matter. 2019;15:2791–2797.

[21] Petelin A. Cross-differential dynamic microscopy v. 0.2 [Internet]. 2020 [cited 2021 Mar 8]. Available from: https://zenodo.org/record/3800382#.YEXzkGhKgzU

[22] Giavazzi F, Crotti S, Speciale A, et al. Viscoelasticity of nematic liquid crystals at a glance. Soft Matter. 2014;10:3938.

[23] Mertelj A, Osterman N, Lisjak D, et al. Magneto-optic and converse magnetoelectric effects in a ferromagnetic liquid crystal. Soft Matter. 2014;10:9065–9072.

[24] Frisch MJ, Trucks GW, Schlegel HB, et al. Gaussian 09, Revision A.02. Gaussian, Inc; Wallingford CT; 2016.

[25] Zhao Y, Truhlar DG. Density functional for spectroscopy: no long-range self-interaction error, good performance for Rydberg and charge-transfer states, and better performance on average than B3LYP for ground states. J Phys Chem A. 2006;110:13126–13130.

[26] Grimme S, Antony J, Ehrlich S, et al. A consistent and accurate ab initio parametrization of density functional dispersion correction (DFT-D) for the 94 elements H-Pu. J Chem Phys. 2010;132:154104.

[27] Kendall RA, Dunning TH, Harrison RJ. Electron affinities of the first-row atoms revisited. Systematic basis sets and wave functions. J Chem Phys. 1992;96:6796–6806.

[28] Mandle RJ, Sebastián N, Martinez-Perdiguero J, et al. On the molecular origins of the ferroelectric splay nematic phase. ArXiv201102722 Cond-Mat [Internet]. 2020 [cited 2021 Feb 13]. Available from: http://arxiv.org/abs/2011.02722 .

[29] Chen X, Korblova E, Glaser MA, et al. Polar in-plane surface orientation of a ferroelectric nematic liquid crystal: polar monodomains and twisted state electro-optics. Proc Natl Acad Sci [Internet]. 2021 [cited 2021 May 31];118. Available from: https://www.pnas.org/content/118/22/e2104092118

[30] de Gennes PG, Prost J. The physics of liquid crystals. Oxford: Clarendon Press; 1995.

[31] Liu Q, Ackerman PJ, Lubensky TC, et al. Biaxial ferromagnetic liquid crystal colloids. Proc Natl Acad Sci. 2016;113:10479–10484.

[32] Rosso R. Orientational order parameters in biaxial nematics: polymorphic notation. Liq Cryst. 2007;34:737–748.

[33] Longa L, Trebin H-R. Theory of liquid crystalline phases in biaxial systems. Mol Cryst Liq Cryst Sci Technol Sect Mol Cryst Liq Cryst. 1992;212:115–124.